



OPEN

A new non-destructive readout by using photo-recovered surface potential contrast

SUBJECT AREAS:
INFORMATION STORAGE
APPLIED PHYSICSReceived
25 July 2014Accepted
21 October 2014Published
10 November 2014Correspondence and
requests for materials
should be addressed to
K.-J.J. (kjjin@iphy.ac.
cn)Le Wang¹, Kui-juan Jin^{1,2}, Jun-xing Gu¹, Chao Ma¹, Xu He¹, Jiandi Zhang³, Can Wang¹, Yu Feng¹, Qian Wan¹, Jin-an Shi¹, Lin Gu¹, Meng He¹, Hui-bin Lu¹ & Guo-zhen Yang^{1,2}¹Institute of Physics, Chinese Academy of Sciences, Beijing 100190, China, ²Collaborative Innovation Center of Quantum Matter, Beijing 100190, China, ³Department of Physics and Astronomy, Louisiana State University, Baton Rouge, LA 70803, USA.

Ferroelectric random access memory is still challenging in the feature of combination of room temperature stability, non-destructive readout and high intensity storage. As a non-contact and non-destructive information readout method, surface potential has never been paid enough attention because of the unavoidable decay of the surface potential contrast between oppositely polarized domains. That is mainly due to the recombination of the surface movable charges around the domain walls. Here, by introducing a laser beam into the combination of piezoresponse force microscopy and Kelvin probe force microscopy, we demonstrate that the surface potential contrast of BiFeO₃ films can be recovered under light illumination. The recovering mechanism is understood based on the redistribution of the photo-induced charges driven by the internal electric field. Furthermore, we have created a 12-cell memory pattern based on BiFeO₃ films to show the feasibility of such photo-assisted non-volatile and non-destructive readout of the ferroelectric memory.

Ferroelectric materials are promising candidates for ferroelectric random access memories (FeRAMs) using their spontaneous polarization¹, which can be switched by an external electrical field. Although FeRAMs are non-volatile and the reading/writing process can be completed within nanoseconds^{2,3}, one fatal problem for conventional FeRAMs is that the reading process, which is performed by applying a bias to the ferroelectric capacitor and detecting the polarization switching current, is destructive because a rewriting process is needed. Thus, it is highly desirable to have a non-destructive readout method^{4–6}.

Polarization reversal influences the surface potential (SP)⁷ which mirrors the surface charges in the polarized regions. A clear understanding of the behavior of surface charges after poling is crucial to utilizing ferroelectricity at the nanometer scale. Despite much of the work on the study of the SP of the ferroelectric materials^{8–12}, relatively little emphasis has been placed on the readout method by measuring the non-contact SP in a ferroelectric memory, simply because the SP contrast (Δ SP) between oppositely polarized domains decays and fails to be kept as a memory, which is mainly due to the evolution and recombination of the movable surface charges^{7,8,11,13} around the domain walls. So far, the room-temperature stability of Δ SP has not been succeeded, so the high density memory based on this concept faces critical challenge.

By introducing a laser beam with an optical fiber into a system for piezoresponse force microscopy (PFM) and Kelvin probe force microscopy (KPFM), we demonstrate conceptually the decay issue of Δ SP between the oppositely polarized domains can be resolved by photo-assisted recovery. Under the sustained internal polarization field, photo-induced charges recover Δ SP, thus reproducing the memory readout signal in a non-destructive and non-volatile manner. Our theoretical calculations reproduce our experimental results, revealing the basic mechanism.

Results and Discussion

Samples preparation and characterizations. 18-nm-thick and 50-nm-thick BiFeO₃ (BFO) films were deposited on the (001)-oriented SrTiO₃ (STO) substrates with a 35-nm-thick SrRuO₃ (SRO) buffer layer by Laser molecular-beam epitaxy (Laser-MBE) technique. Details on film growth and structure are given in the Methods section and Supplementary Information (see Supplementary Fig. S1). Figure 1a presents the cross-sectional high-angle annular dark-field scanning transmission electron microscopy (HAADF-STEM) image of a

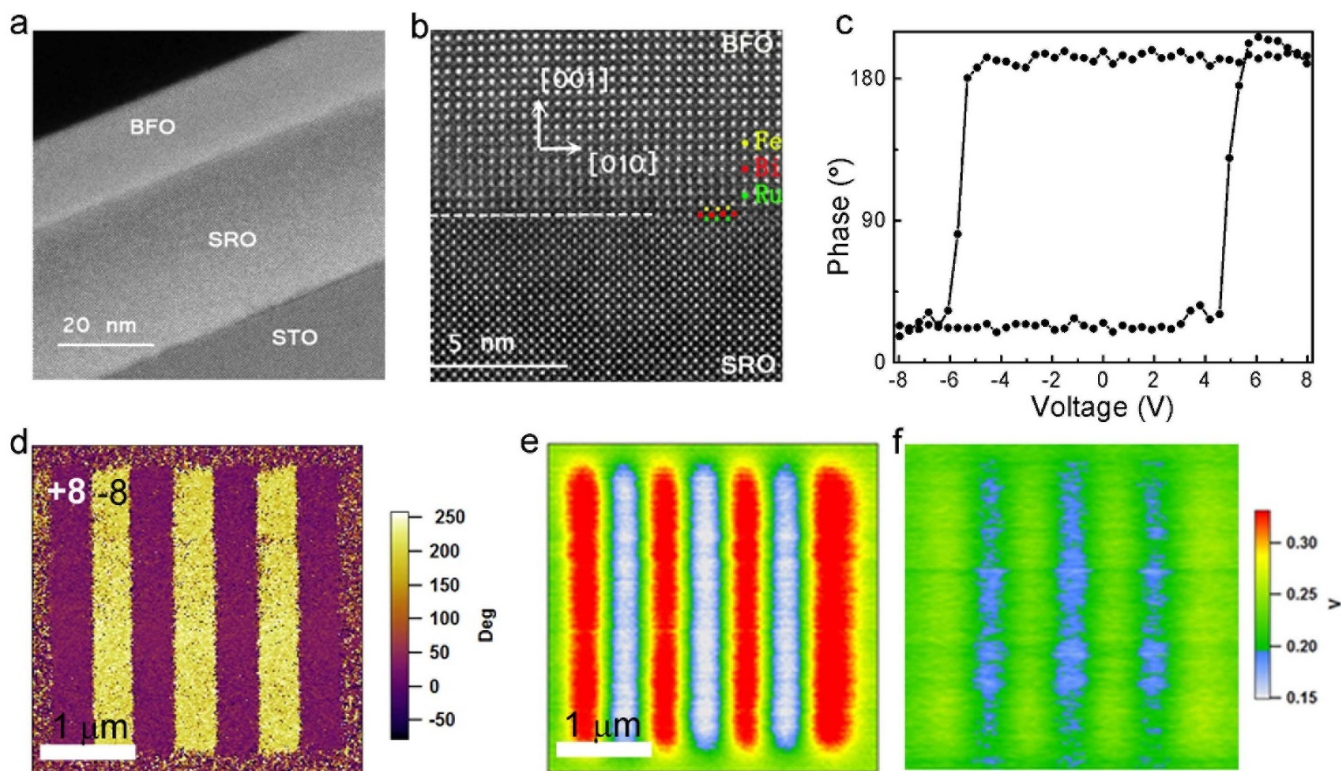


Figure 1 | Samples preparation and characterization. (a) HAADF-STEM image of a BFO/SRO/STO heterostructure. The thicknesses of BFO and SRO layers are 18 and 35 nm, respectively. (b) Cross-sectional HAADF-STEM image for the BFO/SRO interface. (c) Local PFM hysteresis loops measured in the 18-nm-thick BFO film. (d) Out-of-plane PFM phase image on the stripes written by the PFM tip with +8 V and −8 V bias alternatively. (e) and (f) KPFM image at the same area obtained immediately and 14 hour after poling, respectively.

BFO/SRO/STO heterostructure with 18-nm-thick BFO films. Figure 1b shows a zoom-in cross-sectional HAADF-STEM image of the BFO/SRO interface. The atomic resolved image clearly indicates the high quality of epitaxial heterostructure with well-ordered lattice structure and well defined RuO_2/BiO interface. The STEM analysis shows that BFO epitaxially grown on SRO-covered (001)-oriented STO single crystal substrate exhibits a rhombohedral-like (R-like) c/a ratio around 1.03, which is identical with those reported previously^{14,15}. Good ferroelectric quality of the film and asymmetric coercive fields are evident from the local piezoresponse phase hysteresis shown in Fig. 1c. For the 18-nm-thick BFO films the related coercive fields are $E_C(+)$ = 4.5 V and $E_C(-)$ = −6 V, respectively.

The nanometer scale polarization patterning can be achieved by PFM technique. Polarization pattern with contrast polarization can be created by flipping tip-bias during scanning with a tip-bias voltage larger than the coercive voltage. Figure 1d shows the image of the out-of-plane PFM phase image of the area of BFO film surface after poling with alternative +8 and −8 V bias. Seven $0.5 \mu\text{m} \times 3.5 \mu\text{m}$ well-defined polarized striped domains were formed and the 180° phase contrast reveals that the polarization is antiparallel in the adjacent two polarized domains. The dark regions correspond to the downward-polarized (P_{down}) domains in which polarization vector is oriented to the bottom electrode, while the bright regions represent the upward-polarized (P_{up}) domains. As shown in Fig. 1d, the polarization of the as-grown BFO films on the SRO-covered STO substrates has a preferred downward direction as appeared in dark area of the image¹⁵. After switching the polarization to the downward direction by applying a positive voltage on a conductive tip, positive screen charges are accumulated on the surface of a domain⁷. In contrast, negative screen charges are accumulated on the surface after switching the polarization to the upward direction.

As the readout signal for contrast polarization domains, ΔSP can quantitatively obtained with KPFM technique. KPFM was used to study the surface charges dynamics process by imaging surface screening charge distribution^{10,11}. Figure 1e displays the KPFM image for the patterned area shown in Fig. 1d, both obtained right after sample poling. The difference of imaging contrast reflects the SP difference of patterned domains. Normally the quantitative value of SP is difficult to be determined¹⁶. However, the difference of SP between the nearest oppositely polarized domains, i.e., ΔSP , can be quantitatively measured through the line profile of KPFM image. As shown in Fig. 1e, larger SP (red regions) is observed over the P_{down} domains, while smaller SP (white regions) is observed over the P_{up} domains, indicating that the value of domain-related SP is governed by the screening charges. Similar results were observed on the 50-nm-thick BFO films (see Supplementary Fig. S2). All SPs on our BFO films have positive values regardless of the sign of the applied voltages, which may be related to the choice of zero point of SP or the non-zero SP in the as-grown films⁸. Figure 1f presents the KPFM image of exactly the same area as that in Fig. 1d and 1e but taken after 14 h. The image contrast is greatly reduced, indicating the decay of ΔSP due to the diminishment of the surface screening charges^{13,17,18}.

Surface potential contrast decay and photo-induced recovery.

Such a decay of ΔSP can be revised by photo-induced charge recovery. By introducing a beam of laser to the imaged surface with an optical fiber (see the details in the Supplementary Information), we designed a series of experiments and observed a photo-induced dramatic increase of ΔSP . Figure 2 summarize the results of time-dependence of SP profiles and the photo-induced recovery of ΔSP under light illumination for both 18-nm-thick and 50-nm-thick BFO films. Figure 2a and 2b present the line profiles from the KPFM images taken right after poling, 14 h after poling,

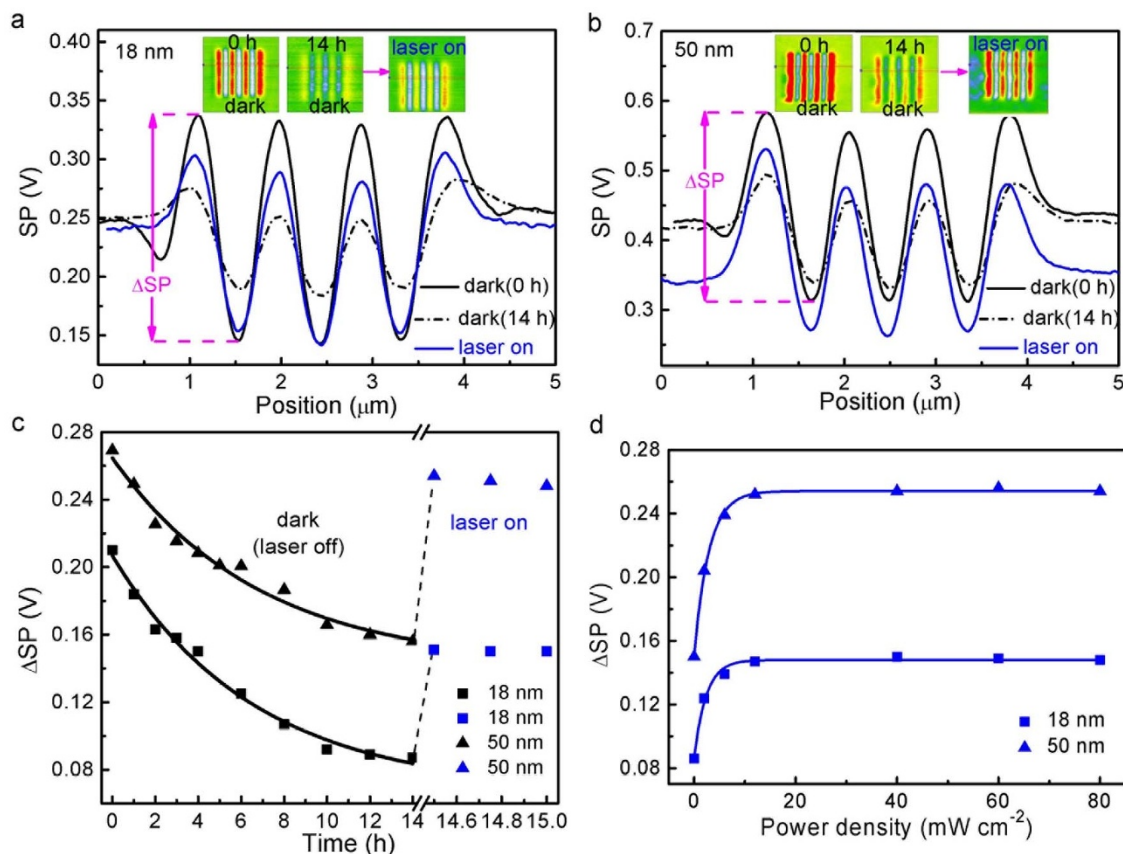


Figure 2 | Photo-induced recovery of the surface potential contrast. Surface potential profiles for (a) 18-nm-thick BFO films and (b) 50-nm-thick BFO films obtained from the inset of KPFM images measured without (dark) and with light illumination by a 375 nm laser (power density of 40 mW cm⁻²). The surface potential contrast between the adjacent oppositely polarized domains is marked. (c) Time dependence and (d) Power density dependence of ΔSP for 18-nm-thick and 50-nm-thick BFO films. Solid lines represent the fitting curves to an exponential decay function, respectively.

and when illuminating with laser light on the sample 14 h after poling. Clearly with light illumination, the ΔSP is almost recovered to its original values, especially for the 50-nm-thick film. In order to gain more quantitative insight into the decaying behavior and the recovery process, we show the time-dependence of measured ΔSP before and after switching on the light illumination and laser power-dependence of ΔSP in Fig. 2c and 2d, respectively. First, we find that the time decay length of ΔSP depends on film thickness. For 18-nm-thick film, the decay length is 6.56 h by fitting the data shown in Fig. 2c to an exponential decay function. For 50-nm-thick film the decay length is 6.85 h. Thus the decay length of ΔSP is a slightly proportional to the film thickness, reflecting dimensionality effect. Second, the recovery of ΔSP under light illumination is also dependent on film thickness. In contrast to 50-nm-thick film where ΔSP is almost fully recovered, the recovery of ΔSP is only about 80% for 18-nm-thick film. Third, we find the recovery is stable as long as the light is on.

As shown in Fig. 2d, ΔSP increases with the power density of the laser and then tends to be saturated when the power density is larger than 20 mW cm⁻², in accordance with the variation of the open circuit voltage in ferroelectric photovoltaic effect^{19,20}. The above observations indicate that the photo-generated electron-hole pairs separated in the films cause the redistribution of surface charges and recover the SP profile on the BFO films. Moreover, we did not observe any noticeable change on SP when the sample was irradiated by a 632.8 nm HeNe laser, which has photon energy smaller than the band gap of BFO. This confirms that the variations of ΔSP under the illumination mainly come from the photovoltaic effect, instead of the thermal effect. Although the variations of ΔSP were observed under the illumination, the domain structure did not show any

obvious change, indicating that illumination did not reorient the ferroelectric domains²¹ and the process is truly non-volatile. Therefore, such a photo-assisted non-destructive readout method by measuring non-contact SP may pave a new pathway to the FeRAMs.

Feasibility of photo-recovered readout method. To demonstrate the possibility of high density memory storage or to further assess the potential of the photo-assisted non-destructive readout method by measuring non-contact surface potential in FeRAMs, we have explored the scalability by writing matrices of square cells and reading their SPs. Figure 3a shows the out-of-plane phase image of a 3 × 4 matrix of 1.1 μm × 1.1 μm cell written alternately at +9.8 and -9.8 V for 50-nm-thick BFO films. Figure 3b and Fig. 3c displays the SP readout of this matrix measured 0 h and 12 h after the matrix was created, respectively. A distinct decay of ΔSP with time was observed. When the laser (power density of 40 mW cm⁻²) was switched on, ΔSP almost fully recovered to the initial value, as shown in Fig. 3d. The SP profiles obtained from the KPFM images in Figs. 3b–3d clearly show the decay of ΔSP with time and the photo-induced ΔSP recovery, as shown in Fig. 3e and 3f. An exponential decay of ΔSP with time is evident. The decay length is 2.98 h by fitting the data shown in Fig. 3f to an exponential decay function. Comparing with the decay length of 6.85 h in the above pattern written with the seven 0.5 μm × 3.5 μm strips in the BFO films with the same thickness of 50 nm, we can clearly see that the decay length of ΔSP is also proportional to the domain size. Furthermore, by turning laser on and off for a couple of times we find that the photo-induced recovery of ΔSP is quite repeatable as shown in Fig. 3f. This further confirms that the ferroelectric photovoltaic effect on BFO films plays an important role in the above observed

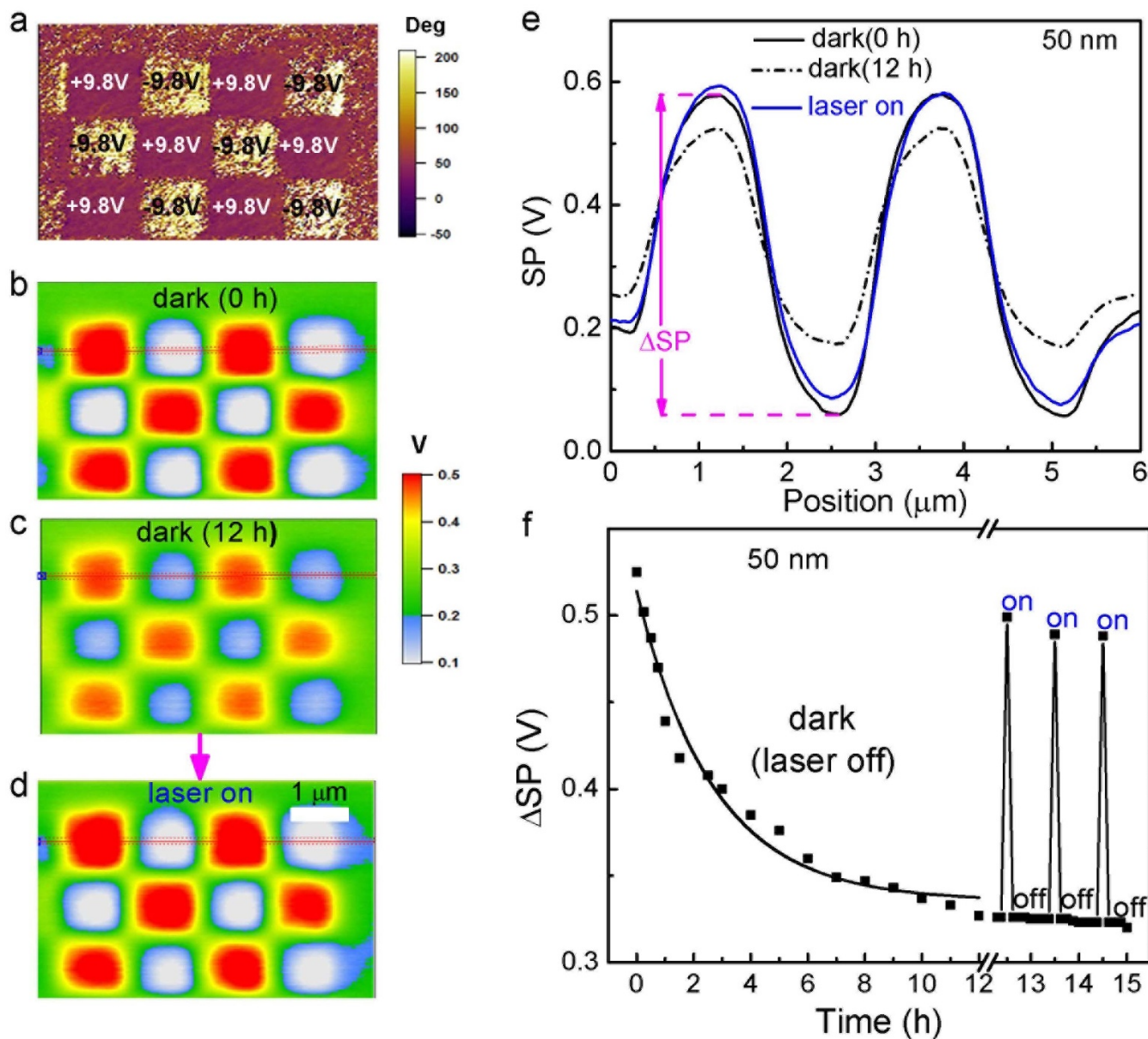


Figure 3 | Feasibility demonstration of the photo-assisted non-destructive readout method. (a) Out-of-plane PFM phase image obtained after poling for 50-nm-thick BFO films with polarized pattern. (b)–(d) KPFM images measured without (dark) and with light illumination by a 375 nm laser (power density of 40 mW cm^{-2}). (e) Surface potential profiles obtained from (b)–(d), respectively. (f) Time dependence of ΔSP . “on” and “off” represent laser on and laser off, respectively. The solid line is the fitting curve to an exponential function.

phenomena. The results demonstrate the feasibility of the photo-assisted non-destructive readout method by measuring non-contact SP in FeRAMs.

Discussion. In order to understand the photo-induced large increase and recovery of the ΔSP from decay, the schematic interfacial band diagrams are sketched in Figs. 4a–4c. According to the work function (about 5.2 eV) of the bottom bulk electrode SRO²² and the affinity (3.3 eV) of bulk BFO²³, a Schottky barrier (about 1.9 eV height) at the BFO/SRO interface can be estimated in the as-grown state shown in Fig. 4a. The polarization of BFO films can be switched by using different directions of bias in the writing (poling) process. Polarization reversal will result in two band bending states and two corresponding internal electrical fields (illustrated in Fig. 4b and Fig. 4c)^{24–26}, thus creating the difference of surface potential or surface potential contrast, ΔSP . However, ΔSP is not stable due to the decay of surface screen charges. As we have described above, the

exponential decay length depends on film thickness, 6.56 h for 18-nm-thick film and 6.85 h for 50-nm-thick film, respectively. As shown in Fig. 2c, the illumination of laser can instantaneously bring back ΔSP . The recovery of ΔSP with laser illumination happens with μs time scale, and within this process the separated photo-generated electron-hole pairs are driven by residual internal polarized field in BFO films. As long as the photon energy of laser is larger than the band gap of BFO, the non-equilibrium photo-generated carriers can be uniformly generated over the BFO films under the illumination and do not massively recombine within the domains^{27,28}. For the P_{down} state with positive SP shown in Fig. 4b, the internal electrical field can drive the photo-generated electrons to the BFO/SRO interface, and these electrons are collected by the bottom electrode, while the photo-generated holes move to the BFO film surface, which leads to the increase of the SP (i.e., more positive) in the P_{down} domains. In contrast, for the P_{up} state with negative SP shown in Fig. 4c, the photo-generated electrons will be

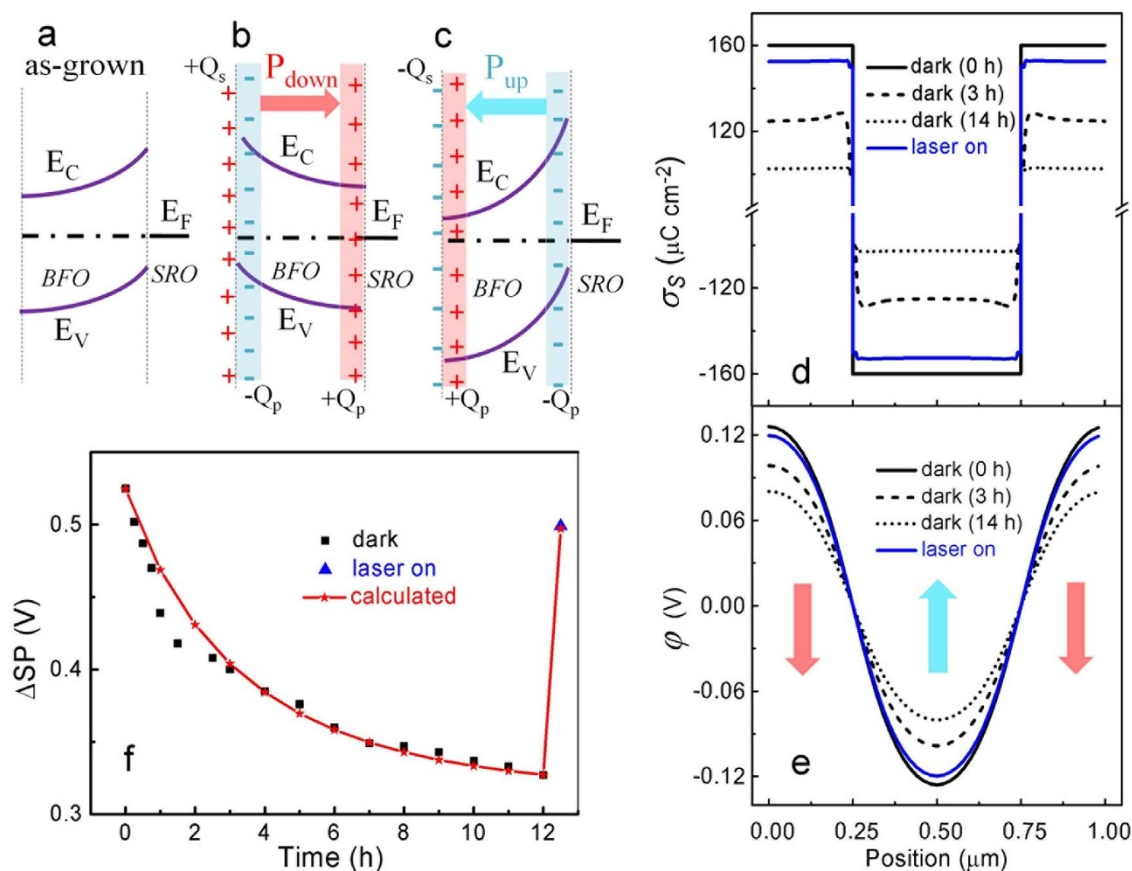


Figure 4 | Results of theoretical calculations. Schematic band diagrams illustrating the variations in Schottky barriers at (a) as-grown state, (b) P_{down} state, and (c) P_{up} state, respectively. Where, E_C , E_V , and E_F denote the conduction band, valence band, and Fermi level of oxide, respectively; Q_p denotes the polarization charge and Q_s the surface screen charge. (d) Calculated screening charge density profile σ_s . (e) Calculated SP (ϕ at $z = 40$ nm) evolution. The arrows represent the polarization direction. (f) Calculated time dependence of ΔSP compared with the experimental data for the 50-nm-thick BFO films. The detailed description of ΔSP calculations can be found in the Supplementary Information.

driven by the internal electrical field to the surface, leading to the decrease of the SP (i.e., more negative). Reversal internal electrical fields in the oppositely polarized domains lead to an opposite change of SP under the illumination. Therefore, ΔSP can be fully recovered under the laser illumination. ΔSP can further increase with the power density, and eventually tend to be saturated when the generation rate of photo-generated electron-hole pair equals to the recombination rate. For 50-nm-thick BFO films, the more apparent recovery of ΔSP from decay under the illumination should be caused by the larger internal electrical field due to the wider depletion region with larger effective area of absorption light and more photo-generated carriers²⁹.

To confirm the above physical scenario, a numerical calculation based on a one-dimensional time-dependent drift diffusion (1DTDDD) model has been carried out^{30–32}. Detailed descriptions of the numerical model and ΔSP calculation can be found in the Supplementary Information. The calculated distribution of the screening charge density of polarized domains and the corresponding SP evolution for different time periods after poling as well as that under the light illumination are shown in Fig. 4d and 4e, respectively. These theoretical results reproduce well the experimental data, as shown in Fig. 4f. The over-screened surface charges, which mainly come from the charge injection effect by the conductive probe in the writing process³³, can drift, diffuse, and recombine. The injected charges only exist on the surface oppositely distributed for the nearest domains. Therefore, in a single domain, there is no corresponding opposite free charges in the film or at the interface to recombine with

these injected charges, which means the injected electrons cannot meet positive charges if they travel along the thickness direction. As electrons need to cross the domain walls to meet positive charges, this process happens in the direction of crossing the domain walls, parallel to the surface, in a scale of μm . The attractive force from the oriented dipoles has a strong effect on the spread of the charge on ferroelectric films⁷. Our calculation results also show that the potential barrier (about 0.3 eV) at domain boundaries will hinder the spread of the surface charges. Therefore, after the application of bias voltage, the relaxation of SP is very slow in our experimental results. Different with the slow relaxation process of the injected charges from the conductive probe, the lifetime of photo-generated carriers on the BFO films is much more faster (about 100~200 ns³⁴). With switching on the laser, the generation rate is much higher than the recombination rate²⁷. Therefore, we observed the rapid recovery of ΔSP from the decay. If we keep the laser switching on, the generation and recombination rates will be equal, thus we observed the ΔSP kept almost constant as shown in Fig. 2c. When we switch off the laser, the generation rate becomes zero and only recombination processes take place. As electrons and holes are generated in pairs and driven in the reverse direction perpendicular to the surface, within this recombination process, electrons only need to travel within 50 nm (the thickness of films) to meet holes. This happens within a single domain, without any barrier from domain boundaries to cause further delay of recombination. Therefore, when switching off the laser, photo-generated non-equilibrium electron-hole pairs can recombine so much faster, ΔSP immediately goes back to the original value, as



shown in Fig. 3f. This photo-induced recovery of Δ SP reproduces the memory readout signal in a non-destructive and non-volatile manner.

Summary. By introducing light illumination, we have demonstrated that the surface potential contrast between the adjacent oppositely polarized domains can be recovered based on the mechanism of ferroelectric photovoltaic effect. The redistribution of the photo-induced charges driven by the internal electric field is the origin of the increase and recovery of the surface potential contrast. With this mechanism, our theoretical calculations reproduce the observed experimental data. Therefore, a novel photo-assisted non-destructive readout method in BFO thin film by using non-contact surface potential can be realized as non-volatile ferroelectric memory, thus resolving a long standing issue existing in FeRAMs.

Methods

Sample preparation. Laser molecular-beam epitaxy (Laser-MBE) technique was used to prepare the SrRuO₃ bottom electrode and epitaxial BiFeO₃ films. The 35-nm-thick SrRuO₃ layer was first grown on the (001)-oriented SrTiO₃ single crystal substrate. The BiFeO₃ layer (18-nm-thick or 50-nm-thick) was subsequently deposited in the same system. Both SrRuO₃ and BiFeO₃ were deposited at 580°C with the oxygen pressure of 10 Pa. A XeCl 308 nm excimer laser was used with an energy density of ~ 2 J cm⁻² and a repetition rate of 2 Hz. After deposition, the samples were *in-situ* annealed for 20 min, and then cooled down to room temperature. Thickness was determined via measurement of transmission electron microscope (TEM).

Structure characterization. The x-ray diffraction (XRD) patterns (Supplementary Figure S1) are performed by a Huber 5021 six-axes diffractometer using a 1.24 Å wavelength at the Shanghai Synchrotron Radiation Facility (SSRF). The high-angle annular-dark-field (HAADF) micrographs of the as-grown BFO films were used an ARM-200F (JEOL, Tokyo, Japan) scanning transmission electron microscope (STEM) operated at 200 kV with a CEOS Cs corrector (CEOS GmbH, Heidelberg, Germany) to cope with the probe-forming objective spherical aberration. The attainable resolution in HAADF images is better than 0.1 nm.

Piezoresponse Force Microscopy (PFM) and Kelvin probe force microscopy (KPFM). PFM and KPFM images were recorded using a commercial atomic force microscopy (AFM) system (Asylum Research MFP3D). PFM technique was used to obtain the well-defined domains, and then KPFM technique was used to study the variations of the surface potential after poling. The relative humidity and temperature remained unchanged in the measurement process. Pt-coated conductive tips (Olympus AC240, a spring constant of ~ 2 N m⁻¹ and a free air resonance frequency of ~ 70 kHz) were used for the scanning. Samples poling were performed in the lithography mode by applying a voltage to the tip during the scanning. The scanning rates of writing bitmap and reading bitmap were 0.4 and 1 Hz, respectively. The voltage of the reading bitmap was 0.8 V. The surface potential signal was recorded in successive scans in the dark or under steady-state illumination using a non-contact mode. The scanning rate was 0.5 Hz. The tip lift height is about 40 nm for KPFM measurements. The sample under the conductive tip was illuminated by a continuous laser (Oxxius, power density of 0–80 mW cm⁻²) of 375 nm wavelength ($h\nu = 3.31$ eV) focused into a circle spot with a diameter of ~ 0.3 mm (see Supplementary Fig. S3) or a continuous laser (Newport Corporation, power density of 20 mW cm⁻²) of 632.8 nm wavelength ($h\nu = 1.96$ eV).

- Ramesh, R. & Spaldin, N. A. Multiferroics: progress and prospects in thin films. *Nat. Mater.* **6**, 21–29 (2007).
- Scott, J. Data storage: Multiferroic memories. *Nat. Mater.* **6**, 256–257 (2007).
- Rana, D. S. *et al.* Understanding the nature of ultrafast polarization dynamics of ferroelectric memory in the multiferroic BiFeO₃. *Adv. Mater.* **21**, 2881–2885 (2009).
- Garcia, V. *et al.* Giant tunnel electroresistance for non-destructive readout of ferroelectric states. *Nature* **460**, 81–84 (2009).
- Kim, D. *et al.* Ferroelectric tunnel memristor. *Nano Lett.* **12**, 5697–5702 (2012).
- Brody, P. Ferroelectric photovoltaic method and apparatus for transferring information. US Patent US4103341 (1978).
- Chen, X. *et al.* Surface potential of ferroelectric thin films investigated by scanning probe microscopy. *J. Vac. Sci. Technol. B* **17**, 1930–1934 (1999).
- Choi, H., Hong, J. & No, K. Local surface potential distribution and its relaxation in ferroelectric poly(vinylidene fluoride-co-trifluoroethylene) thin films. *Appl. Phys. Lett.* **101**, 042904 (2012).
- Kalinin, S. V. & Bonnell, D. A. Local potential and polarization screening on ferroelectric surfaces. *Phys. Rev. B* **63**, 125411 (2001).
- Kalinin, S. V. & Bonnell, D. A. Screening phenomena on oxide surfaces and its implications for local electrostatic and transport measurements. *Nano Lett.* **4**, 555–560 (2004).

- Kim, Y. *et al.* Local surface potential distribution in oriented ferroelectric thin films. *Appl. Phys. Lett.* **91**, 052906 (2007).
- Yan, F., Chen, G., Lu, L. & Spanier, J. E. Dynamics of Photogenerated Surface Charge on BiFeO₃ Films. *ACS nano* **6**, 2353–2360 (2012).
- Zhang, Q., Kim, C., Jang, Y., Hwang, H. & Cho, J. Multiferroic properties and surface potential behaviors in cobalt-doped BiFeO₃ film. *Appl. Phys. Lett.* **96**, 152901 (2010).
- Dupé, B. *et al.* Competing phases in BiFeO₃ thin films under compressive epitaxial strain. *Phys. Rev. B* **81**, 144128 (2010).
- Johann, F., Morelli, A., Biggemann, D., Arredondo, M. & Vrejoiu, I. Epitaxial strain and electric boundary condition effects on the structural and ferroelectric properties of BiFeO₃ films. *Phys. Rev. B* **84**, 094105 (2011).
- Segura, J., Domingo, N., Fraxedas, J. & Verdaguer, A. Surface screening of written ferroelectric domains in ambient conditions. *J. Appl. Phys.* **113**, 187213 (2013).
- Tzeng, S.-D. & Gwo, S. Charge trapping properties at silicon nitride/silicon oxide interface studied by variable-temperature electrostatic force microscopy. *J. Appl. Phys.* **100**, 023711 (2006).
- Verdaguer, A. *et al.* Charging and discharging of graphene in ambient conditions studied with scanning probe microscopy. *Appl. Phys. Lett.* **94**, 233105 (2009).
- Ji, W., Yao, K. & Liang, Y. C. Bulk photovoltaic effect at visible wavelength in epitaxial ferroelectric BiFeO₃ thin films. *Adv. Mater.* **22**, 1763–1766 (2010).
- Guo, R. *et al.* Non-volatile memory based on the ferroelectric photovoltaic effect. *Nat. Commun.* **4**, 1990 (2013).
- Shao, R., Nikiforov, M. P. & Bonnell, D. A. Photoinduced charge dynamics on BaTiO₃ (001) surface characterized by scanning probe microscopy. *Appl. Phys. Lett.* **89**, 112904 (2006).
- Fang, X. & Kobayashi, T. Study of pulsed laser deposition of RuO₂ and SrRuO₃ thin films. *Appl. Phys. A* **69**, S587–S590 (1999).
- Clark, S. & Robertson, J. Band gap and Schottky barrier heights of multiferroic BiFeO₃. *Appl. Phys. Lett.* **90**, 132903 (2007).
- Huang, B. *et al.* Direct observation of ferroelectric polarization-modulated band bending at oxide interfaces. *Appl. Phys. Lett.* **100**, 122903 (2012).
- Wang, C. *et al.* Switchable diode effect and ferroelectric resistive switching in epitaxial BiFeO₃ thin films. *Appl. Phys. Lett.* **98**, 192901 (2011).
- Ge, C. *et al.* Numerical investigation into the switchable diode effect in metal-ferroelectric-metal structures. *Appl. Phys. Lett.* **99**, 063509 (2011).
- Alexe, M. Local mapping of generation and recombination lifetime in BiFeO₃ single crystals by scanning probe photoinduced transient spectroscopy. *Nano Lett.* **12**, 2193–2198 (2012).
- Alexe, M. & Hesse, D. Tip-enhanced photovoltaic effects in bismuth ferrite. *Nat. Commun.* **2**, 256 (2011).
- Zhang, J. *et al.* Enlarging photovoltaic effect: combination of classic photoelectric and ferroelectric photovoltaic effects. *Sci. Rep.* **3**, 2109 (2013).
- He, X. *et al.* The mechanism of the maximum photovoltage in perovskite oxide heterostructures with the critical thickness. *Europhys. Lett.* **102**, 37007 (2013).
- Liao, L. *et al.* Theoretical study on the photodoping effects in La_{1-x}Sr_xMnO₃/SrNb₂Ti_{1-x}O₃ p-n heterojunction. *Phys. Status Solidi A* **206**, 1655–1659 (2009).
- Selberherr, S. *Analysis and simulation of semiconductor devices.* (Springer Wien; New York, 1984).
- Efimov, A. & Cohen, S. R. Simulation and correction of geometric distortions in scanning Kelvin probe microscopy. *J. Vac. Sci. Tech. A* **18**, 1051–1055 (2000).
- Yamada, Y., Nakamura, T., Yasui, S., Funakubo, H. & Kanemitsu, Y. Measurement of transient photoabsorption and photocurrent of BiFeO₃ thin films: Evidence for long-lived trapped photocarriers. *Phys. Rev. B* **89**, 035133 (2014).

Acknowledgments

This work was supported by the National Basic Research Program of China (Nos. 2014CB921000 and 2012CB921403), the National Natural Science Foundation of China (Nos. 11134012 and 11174355), and the Strategic Priority Research Program (B) of the Chinese Academy of Sciences (No. XDB07030200). The XRD measurements were supported by Shanghai Synchrotron Radiation Facility.

Author contributions

L.W., K.J. and J.G. contributed equally to this work. K.J. contributed the whole idea and designed the experiments. L.W., J.G., Y.F., M.H., H.L. and G.Y. prepared the films and devices. L.W., J.G. and C.W. conducted the PFM and KPFM experiments. C.M. and X.H. performed the theoretical analysis. Q.W. performed the XRD test and analysis. J.S. and L.G. helped to collect and analyze the TEM images. K.J., L.W., J.G. and J.Z. wrote the paper. All authors discussed the results and commented on the manuscript.

Additional information

Supplementary information accompanies this paper at <http://www.nature.com/scientificreports>

Competing financial interests: The authors declare no competing financial interests.

How to cite this article: Wang, L. *et al.* A new non-destructive readout by using photo-recovered surface potential contrast. *Sci. Rep.* **4**, 6980; DOI:10.1038/srep06980 (2014).



This work is licensed under a Creative Commons Attribution-NonCommercial-ShareAlike 4.0 International License. The images or other third party material in this article are included in the article's Creative Commons license, unless indicated otherwise in the credit line; if the material is not included under the Creative

Commons license, users will need to obtain permission from the license holder in order to reproduce the material. To view a copy of this license, visit <http://creativecommons.org/licenses/by-nc-sa/4.0/>